New insight into CO_2-mediated denitrification process in H_2-based membrane biofilm reactor

An experimental and modeling study

Jiang, Minmin; Zheng, Junjian; Perez-Calleja, Patricia; Picioreanu, Cristian; Lin, Hua; Zhang, Xuehong; Zhang, Yuanyuan; Li, Haixiang; Nerenberg, Robert

DOI
10.1016/j.watres.2020.116177

Publication date
2020

Document Version
Final published version

Published in
Water Research

Citation (APA)
Jiang, M., Zheng, J., Perez-Calleja, P., Picioreanu, C., Lin, H., Zhang, X., Zhang, Y., Li, H., & Nerenberg, R. (2020). New insight into CO_2-mediated denitrification process in H_2-based membrane biofilm reactor: An experimental and modeling study. *Water Research*, *184*, Article 116177. https://doi.org/10.1016/j.watres.2020.116177

Water Research 184 (2020) 116177

Contents lists available at ScienceDirect

Water Research

journal homepage: www.elsevier.com/locate/watres

New insight into CO_2-mediated denitrification process in H_2-based membrane biofilm reactor: An experimental and modeling study

Minmin Jiang[a,c,1], Junjian Zheng[b,1], Patricia Perez-Calleja[c], Cristian Picioreanu[d], Hua Lin[a], Xuehong Zhang[a], Yuanyuan Zhang[b], Haixiang Li[a,*], Robert Nerenberg[c,*]

[a] Guilin University of Technology, College of Environmental Science and Engineering, 319 Yanshan Street, Guilin, 541006, China
[b] Guilin University of Electronic Technology, College of Life and Environmental Science, 1 Jinji Road, Guilin, 541004, China
[c] University of Notre Dame, Department of Civil and Environmental Engineering and Earth Sciences, 156 Fitzpatrick Hall, Notre Dame, IN, 46556, USA
[d] Department of Biotechnology, Faculty of Applied Sciences, Delft University of Technology, Van der Maasweg 9, 2629 HZ, Delft, the Netherlands

ARTICLE INFO

Article history:
Received 28 February 2020
Revised 7 July 2020
Accepted 12 July 2020
Available online 13 July 2020

Keywords:
H_2-based membrane biofilm reactor (H_2−MBfR)
Denitrification
CO_2 addition
Mathematical model

ABSTRACT

The H_2-based membrane biofilm reactor (H_2−MBfR) is an emerging technology for removal of nitrate (NO_3^-) in water supplies. In this research, a lab-scale H_2−MBfR equipped with a separated CO_2 providing system and a microsensor measuring unit was developed for NO_3^- removal from synthetic groundwater. Experimental results show that efficient NO_3^- reduction with a flux of 1.46 g/(m^2·d) was achieved at the optimal operating conditions of hydraulic retention time (HRT) 80 min, influent NO_3^- concentration 20 mg N/L, H_2 pressure 5 psig and CO_2 addition 50 mg/L. Given the complex counter-diffusion of substrates in the H_2−MBfR, mathematical modeling is a key tool to both understand its behavior and optimize its performance. A sophisticated model was successfully established, calibrated and validated via comparing the measured and simulated system performance and/or substrate gradients within biofilm. Model results indicate that i) even under the optimal operating conditions, denitrifying bacteria (DNB) in the interior and exterior of biofilm suffered low growth rate, attributed to CO_2 and H_2 limitation, respectively; ii) appropriate operating parameters are essential to maintaining high activity of DNB in the biofilm; iii) CO_2 concentration was the decisive factor which matters its dominant role in mediating hydrogenotrophic denitrification process; iv) the predicted optimum biofilm thickness was 650 μm that can maximize the denitrification flux and prevent loss of H_2.

1. Introduction

Nitrate (NO_3^-) contamination of groundwater, primarily from anthropogenic activities such as intensive agricultural practices, on-site wastewater disposal and livestock manure management, has become a worldwide concern (Liu and Wang, 2019; Wakida and Lerner, 2005). In China, 70% of population obtains drinking water from groundwater sources, where fully 90% of shallow groundwater suffers from contamination and where NO_3^- is among the dominant pollutants with typical concentrations ranging from 10 to 100 mg N/L (Qiu, 2011; Su et al., 2013; Gu et al., 2013; Gao et al., 2020). Physicochemical treatment strategies, e.g., adsorption, membrane filtration, electrodialysis, photo-/electro- catalysis and chemical reduction (Cecconet et al., 2018; Sevda et al., 2018), are capable of separating or degrading NO_3^- but have difficulties with large-scale applications due to high energy demand and/or requirements of post-treatment steps, as a result of inefficient transformation of NO_3^- into innocuous N_2 or chemical residue occurrence in treated water. Heterotrophic denitrification is effective for denitrification but is rarely used due to the need to add organic electron donors, which are often expensive, toxic, have handling concerns, and require post treatment (Cecconet et al., 2018).

The H_2-based membrane biofilm reactor (H_2−MBfR) is an emerging biological system based on autotrophic denitrification (Wu et al., 2018). It is preferable over heterotrophic denitrification, as it uses nontoxic and inexpensive H_2 as electron donor and inorganic carbon as carbon source (Nerenberg and Rittmann, 2004). It provides high NO_3^- removal fluxes, low residual organics and biomass as well as minimal H_2 loss in the effluent (if designed and operated appropriately, H_2 can be fully utilized), and the reduction of co-occurring oxidized contaminants (e.g., perchlo-

* Corresponding authors.
E-mail addresses: 2011042@glut.edu.cn (H. Li), nerenberg.1@nd.edu (R. Nerenberg).
[1] These authors contributed to the work equally and should be regarded as co-first authors.

https://doi.org/10.1016/j.watres.2020.116177
0043-1354/

rate) into innocuous forms (Lee and Rittmann, 2000; Ziv-El and Rittmann, 2009; Wu et al., 2018). In the past decades, a growing body of literature has investigated and/or simulated the performance of H_2−MBfR for a variety of oxidized contaminants elimination (Karanasios et al., 2010; Martin and Nerenberg, 2012; Wu et al., 2018), which has extended our knowledge on theoretical and practical implications of this technology. So far, however, the further development and scale-up application of H_2−MBfR still faces challenges such as scalable process design, effective biofilm management, and a clear understanding of the fundamental principles of biofilm behavior (Chen et al., 2019; Martin and Nerenberg, 2012).

One of most significant characteristics of H_2−MBfR is that hydrogenotrophic denitrification induces the alkalization of the bulk liquid and increases the pH within the biofilm (Lee and Rittmann, 2003; Rittmann and McCarty, 2012). The optimal pH range for hydrogenotrophic denitrification has been reported to be 7.0~9.0, and a pH outside this range may result in lowered denitrification rates, the production of undesirable intermediates (e.g., NO_2^-, NO and N_2O), or membrane fouling due to precipitation of existing hardness cations (Wu et al., 2018; Tang et al., 2011). Proven approaches to pH control in H_2−MBfR involve the addition of phosphate buffer (Ontiveros-Valencia et al., 2012), bicarbonate (Sahu et al., 2009), hydrochloric acid (Ziv-El and Rittmann, 2009) and CO_2 (Tang et al., 2011). It has been conclusively shown that CO_2 addition is a more attractive choice for H_2-based autotrophic process (Wu et al., 2018; Tang et al., 2011). Difficulties arise, however, in attempts to establish effective measures for precise supply of CO_2 in H_2−MBfR. An inadequate supply of CO_2 does not provide sufficient alkalinity neutralization, while excessive CO_2 leads to acidification of bulk liquid, decrease denitrification efficiencies and may have irreversible damage to the system (Ghafari et al., 2009).

More recently, Xia et al. proposed a novel H_2−MBfR in which two bundles of hollow fiber membranes (HFMs) were placed in one flow-cell for bubbleless H_2 and CO_2 supply, and the CO_2 dosage was deduced according to diffusion coefficient calculation of HFM (Xia et al., 2015, 2016). However, such an integrated system has several practical limitations if it is applied for real groundwater treatment. For instance, it will increase the difficulty in the precise addition of CO_2 and impede the trans-membrane tranfer of CO_2 across the HFMs, since the unavoidable occurrence of membrane fouling and biofilm growth on CO_2 HFMs shall cause the uncertainty in how much CO_2 can tranfer into bulk liquid, and the increase in the intra-membrane pressure; once the leakage of CO_2 HFMs happens, the rapid pH drop may greatly impair the microbial activity. Alternatively, a separated CO_2 providing system can avoid above issues. Moreover, a mathematical model that qualitatively and quantitatively assesses the biomass spatial distribution as well as the interaction mechanisms of microorganisms in biofilm during the CO_2-mediated hydrogenotrophic denitrification process has not yet been established.

Herein, we reported an innovative H_2−MBfR which is connected to a separated CO_2 providing system for precise addition of CO_2, and equipped with a microsensor measuring unit for in situ monitoring of H_2 and NO_3^- concentrations inside the biofilm. The effectiveness for NO_3^- removal and the microbial activity were investigated and simulated systematically by means of experimental and modeling evaluation. The objectives of this work include the following: i) to experimentally evaluate how the system performance correlates with key operating factors of the CO_2 source H_2−MBfR; ii) to use in situ detected substrates gradients in biofilm to calibrate model, and then to reveal the microenvironment (e.g., chemical gradients and microbial communities structure) of biofilm under the optimal operating conditions using the calibrated model; iii) to validate the accuracy of the model, and to employ the model to predict the microenvironment evolutions of biofilm with changing key influence factors; iv) to figure out the optimal biofilm thickness that contributes to efficient NO_3^- removal and allows complete utilization of H_2.

2. Materials and methods

2.1. Experimental set-up

Fig. 1a shows the schematic of the H_2−MBfR system made by square-section glass tubes consisting of a vertically installed main flow-cell (dimension = 10 × 10 mm, length = 350 mm) in which a membrane module containing 32 HFMs (HFM200TL, Mitsubishi Rayon, Japan) was put in the middle, as well as a horizontally installed side flow-cell (dimension = 6 × 6 mm, length = 280 mm) where a single HFM was placed inside, and five microsensor access ports were mounted at the top. The main and side flow-cells were connected to the H_2 tank for pure pressurized H_2 supply and the recirculation loop with a pump (Masterflex pump, L/S 16 tubing, Cole-Palmer, USA) at a recirculation flowrate of 80 mL/min to maintain a completely mixed condition of bulk liquid. Related information regarding physical characteristics of the H_2−MBfR is summarized in Table S1. As depicted in Fig. 1b, a microsensor measuring unit comprised of a micromanipulator, a computer and microsensors (for details, see Section 2.3), was linked to the side flow-cell through microsensor access ports, with the microsensors were imbedded into the HFM-attached biofilm for in situ quantification of NO_3^- and H_2 inside the biofilm. Note that the flow-cells were designed as square-section instead of circular-section because of the need for facilitating the operation of microscope to guide the orientation and movement of microsensor tip and the precise measurement of biofilm thickness using optical coherence tomography (OCT).

A separated CO_2 providing system was connected to the H_2−MBfR for CO_2 supply (Fig. 1c), in which deionized water was pumped through the glass tube (dimension = 10 × 10 mm, length = 350 mm) equipped with a bundle of 10 HFMs pressurized with pure CO_2, and then the generated CO_2-riched water in the reservoir was transferred to the bottom of the H_2−MBfR. The influent of the H_2−MBfR was a mixture of contaminants-containing water and CO_2-riched water. The precise addition of CO_2 can be realized by adjusting metering valve on the CO_2 tank or altering influent (mixture) composition (i.e., adjusting the ratio between the volume of contaminants-containing water and CO_2-riched water). The total CO_2 dosage was ascertained by theoretical calculation of CO_2 demand for carbon source based on Eq. (1) (detailed derivation process is described in Section S2) and experimental measurement of extra CO_2 demand for pH control. Such an approach of bubbleless CO_2 supply can effectively avoid CO_2 wasting events compared to the CO_2 sparging method that is widely adopted in commercial-scale MBfRs (Tang et al., 2011), and is applicable to match seasonally and spatially fluctuating NO_3^- loadings that frequently appears in real groundwater treatment processes. There is a concern that the H_2−MBfR with a separated CO_2 providing system may cause dilution issue of influent if it is applied for large-scale real groundwater treatment, however, the degree of dilution can be minimized by mixing real groundwater with small volume of water containing high concentration of CO_2, in view of the high solubility of CO_2 in water.

$$4.48H_2+NO_3^-+H^++0.86CO_2 \rightarrow 0.17C_5H_7O_2N+0.41N_2+4.38H_2O \quad (1)$$

The H_2−MBfR was inoculated with 5 mL of activated sludge from South Bend wastewater treatment plant in Indiana, USA. Start-up of the H_2−MBfR began when CO_2 and H_2 were supplied

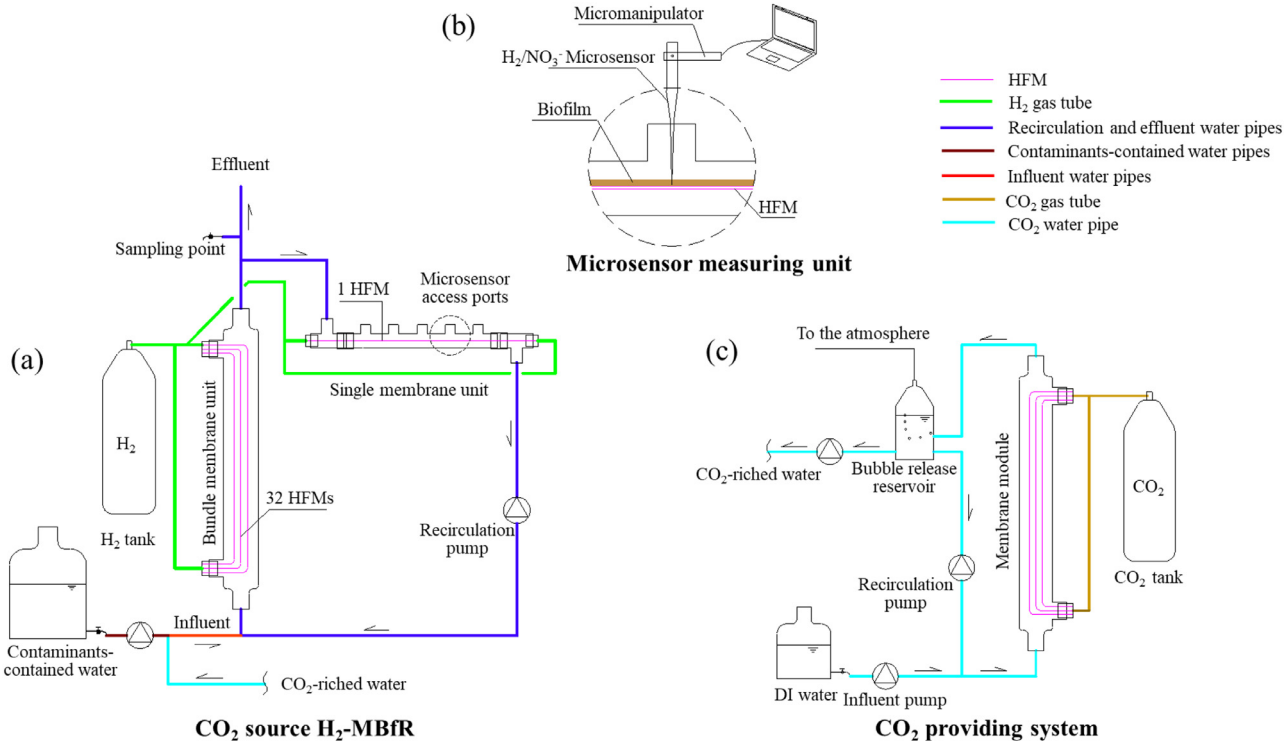

Fig. 1. Schematic representation of the CO_2 source H_2−MBfR set-up. The system consists of three sections: (a) H_2−MBfR: green line indicates H_2 gas tubes while the blue, red and dark red lines are water pipes. (b) details of microsensor measuring unit assembled on the ports of the horizontal glass flow-cell with built-in single HFM. (c) CO_2 providing system: cyan lines represent CO_2-riched water and brown lines are CO_2 gas tubes. (For interpretation of the references to color in this figure legend, the reader is referred to the web version of this article.)

Table 1
Operating conditions for short-term single-factor experiments.

Experiments	Factor	HRT (min)	NO_3^- (mg/L) *	H_2 (psig)	CO_2 (mg/L) *	Bulk liquid pH
HRT series	HRT	***40–180***	20	5.0	50	7.5
NO_3^- series	NO_3^- loading	80	***5–40***	5.0	50	7.5
H_2 series	H_2 pressure	80	20	***1.0–7.0***	50	7.5
CO_2 series	CO_2 addition	80	20	5.0	***5–70***	No adjustment

Note: concentrations of NO_3^-* and CO_2* refer to the final concentration of these compounds that enter the main and side flow-cells after the contaminants-containing water and CO_2-riched water was mixed.

to the reactor at a pressure of 4 and 5 psig, respectively, meanwhile the reactor was operated at room temperature (25 ± 1 °C) and fed with influent (detailed composition can be found in Table S2) at a flow rate of 0.63 mL/min (resulting in a hydraulic retention time (HRT) of 80 min). Although NO_3^- was always recognized as the first electron acceptor in the case of the co-existence of NO_3^- and SO_4^{2-} in H_2−MBfRs (Tang et al., 2013; Zhao et al., 2014; Xia et al., 2013), SO_4^{2-} was added as a co-existing pollutant in the influent due to its ubiquitous presence in real groundwater. After several months of operation, the reactor reached steady-state for NO_3^- removal (20 mg N/L of NO_3^- in the influent could be reduced by ~75%), and the formed biofilm attached on the surface of the single HFM had negligible changes with a thickness of 825 ± 25 μm. It should be emphasized that the 825 μm was the average biofilm thickness at different positions of HFMs, and the small deviation among biofilm thicknesses was perhaps due to the shearing force parallel to the HFMs, the relatively shorter HFMs length and the two-ends gas supply mode. In all assays, aqueous samples collected from the influent and effluent were filtered immediately through a 0.22 μm polyether sulfone membrane filter (VWR, USA), and then stored at 4 °C until analyzed.

2.2. Bio-reduction of NO_3^- experiments

Short-term and long-term single-factor experiments were conducted to investigate how key operating factors affect NO_3^- removal performance of the reactor and/or determine the optimum operating conditions for denitrification. In short-term experiments, four series (i.e., HRT (40−180 min), H_2 pressure (1–7 psig), NO_3^- loading (5–40 mg N/L) and CO_2 addition series (5–70 mg/L)) were tested, for each series, one operating factor varied while maintaining the others fixed (Table 1); aqueous samples were collected from the influent and effluent after the H_2−MBfR was operated for 5–7 HRTs (which is approachable to HRTs used in existing references, e.g., Xia et al., 2016; Zhao et al., 2013a,b). In long-term experiments (in which, operating factor was changed after the maintaining of at least 40 days to allow the H_2−MBfR system to reach steady-state), only the effect of CO_2 addition (10–100 mg/L) variation was evaluated, since the resultant NO_3^- removal fluxes at different CO_2 addition were quite different from those in short-term experiments, while extending the operation period of each of other operating factors from 5–7 HRTs to several days or weeks had negligible influence on the NO_3^- removal fluxes of the system. In par-

ticular, during some long-term experiments, to clarify the role of CO_2 only as carbon source in contributing to NO_3^- removal, the pH of bulk liquid with diverse CO_2 addition was uniformly adjusted to 7.5 by adding 0.1 M HCl or NaOH solution if necessary.

According to the stoichiometric coefficients in Eq. (1), it can be inferred that the theoretical inorganic carbon source demand (measured as C) for 20 mg N/L of NO_3^- reduction is 14.7 mg/L. However, according to our preliminary experimental results, NO_3^- cannot be completely removed, then 13.6 mg/L (measured as C) inorganic carbon source (i.e., 50 mg/L CO_2 or 95 mg/L $NaHCO_3$) was added in the following experiments. Given that HCO_3^- is the dominant existence form of inorganic carbon source in real groundwater (Stumm and Morgan, 1996), and the phosphate buffer (434 mg/L Na_2HPO_4 + 128 mg/L KH_2PO_4) is widely applied for pH control in H_2−MBfR (Chung et al., 2007; Xia et al., 2010), therefore, in order to demonstrate the superiority of CO_2 as the sole carbon source and pH regulator in hydrogenotrophic denitrification process, batch experiments were performed at the optimal operating conditions (ascertained by the results of short-term single-factor experiments) under three scenarios: in Scenarios 1 and 2, the concentration of CO_2 and $NaHCO_3$ in the influent was controlled at 50 and 95 mg/L, respectively, while in Scenario 3, 95 mg/L $NaHCO_3$, 434 mg/L Na_2HPO_4 and 128 mg/L KH_2PO_4 were added to the influent.

2.3. Analytical procedure

The performance of H_2−MBfR for contaminants elimination was evaluated by analyzing the concentrations of NO_3^-, NO_2^- and SO_4^{2-} in influent and effluent. Concentrations of aquatic NO_3^-, NO_2^- and SO_4^{2-} were detected by ion chromatography (ICS-2500, Dionex, USA) coupled with a Dionex AS-19 column (4 × 250 mm, 4 μm) using 55 mM NaOH solution as eluent. The pH of bulk liquid was continuously monitored with a pH meter (Accumet AB250, Fisher Scientific, USA). An acid-base titration method was used to determine the CO_2 concentration in CO_2-riched water (Hach, 1992). The effluent dissolved inorganic carbon (DIC) concentrations were determined by the coulometric method using a UIC CM150 carbon analyzer equipped with a CM5017 CO_2 coulometer (UIC Inc., USA) (Byrne, 2014). Biofilm thickness was detected by OCT (Ganymede-II, Thorlabs, Germany) during the whole experimental period.

Contaminant removal flux (J) in g/(m^2·d) was calculated by Eq. (2) (Lai et al., 2014; Zhao et al., 2014).

$$J = \frac{Q}{A}\left(S_{inf} - S_{\text{eff}}\right) \tag{2}$$

where Q is the influent flow rate (m^3/d), A is the membrane surface area (m^2), S_{inf} and S_{eff} are the contaminant concentrations (g/m^3) of influent and effluent, respectively.

For determination of NO_3^- and H_2 gradients inside biofilm, two types of microsensors were used in the microsensor measuring unit (Fig. 1b), one of which is a $H_2$25 microsensor that is assembled with a microprobe (tip diameter = 20–30 μm) for H_2 detection, was obtained from Unisense A/S Corp. (Denmark); while for measurement of NO_3^-, another potentiometric LIX (liquid ion-exchange) microsensor coupled with a microprobe (tip diameter = 20–50 μm) was prepared according to protocols stated elsewhere (Lewandowski and Beyenal, 2013). The potential difference produced by microsensors was monitored by either a pH/mV meter (Unisense A/S, Dennmark) or a multimeter (Unisense A/S, Dennmark). An automated micromanipulator (Model MM33–2, Unisense A/S, Denmark) equipped with a stereo-zoom light microscope (Cole-Palmer, USA) and a light source (Dolan-Jenner MI-150, Cole-Palmer, USA) was employed to control and visualize the microsensors movement. NO_3^- and H_2 profiles measurements were performed at spatial intervals of 25 μm across the biofilm.

2.4. Mathematical model

2.4.1. Model framework development

Aiming at the in-depth interpretation of microbial metabolic process for contaminants and a better prediction of mechanism-associated components distribution/localization inside biofilm, an optimized mathematical model was developed (detailed information concerning the modeling framework can be found in Section S1), on the basis of a classical one-dimensional (1-D) counter-diffusional biofilm model which is proposed by Rittmann's group (Tang et al., 2012), by introduction into the calculated stoichiometric coefficients (relevant calculation procedure and results can be found in Section S2 and Table S3, respectively), and the expanded process kinetic rate equations. Note that the expansion of the microbial metabolic process kinetics refers to the fact that different from existing models, the synchronous effects of inorganic carbon source and bulk liquid pH on microbial growth were considered in the developed model (see Table S4).

2.4.2. Model solution and calibration

The model solution algorithm was implemented in the AQUASIM 2.1 g simulation platform (Reichert, 1994), by inputting process kinetic rate equations (see Table S4), as well as stoichiometric matrix, stoichiometric parameters and kinetic parameters, experimental parameters, physical parameters, (see Table S3, S5, S6, S7, respectively). Illustration for parameters selection can be found in Section S3. In particular, some parameters (i.e., mass transfer coefficient for H_2 of the HFM (K_{m}), half-maximum-rate concentrations of CO_2 for DNB ($K_{CO_2}^{DNB}$) and sulfate reducing bacteria (SRB) ($K_{CO_2}^{SRB}$)) are unavailable in the literature, and then were estimated by fitting the simulated NO_3^- removal fluxes as well as NO_3^- and H_2 profiles to the experimental measurements at the optimal operating/simulation conditions in this work. Detailed information concerning the calibration and sensitivity analysis of those parameters is described in Section S4.

2.4.3. Model evaluation and validation

The following scenarios were simulated using the calibrated model: i) we simulated steady-state biofilm under the optimal operating conditions to reveal the inherent characteristics of the biofilm of CO_2 source H_2−MBfR in terms of soluble and particulate components profiles, process kinetic rates and particulate compounds distribution, besides comparing the measured and simulated NO_3^- and H_2 gradients/profiles in biofilm and the NO_3^- removal fluxes of the system to preliminarily validate the accuracy of model; ii) effects of key operating factors on characteristics of biofilm with a certain thickness were evaluated by the model, and by comparison of the measured and simulated system performance to further validate the accuracy of model; iii) the measured and simulated NO_3^- removal fluxes and substrates gradients of steady-state biofilms in the cases of inorganic carbon source being and not being considered as a limiting factor were compared to demonstrate the advantage of incorporating the effect of inorganic carbon source on autotrophs growth into microbial metabolic process kinetics; iv) NO_3^- removal fluxes and characteristics evolutions of the steady-state biofilms with different thickness were simulated and compared to elucidate the optimal biofilm thickness based on goodness of performance criterion (Lee and Rittmann, 2002). Overall, six scenarios (Scenarios E1-E6) were simulated for model evaluation (see Table S8). It is worth noting that to further validate the accuracy of model, the experimental measurements in short-term and long-term single-factor experiments were used to compare the model predictions in Scenarios E2-E4 and Scenario E5, respectively; in Scenarios E3 and E4, the measured NO_3^- removal fluxes at H_2 pressure of 3–7 psig and influent NO_3^- concentrations of 10–30 mg N/L were used to validate the model was mainly

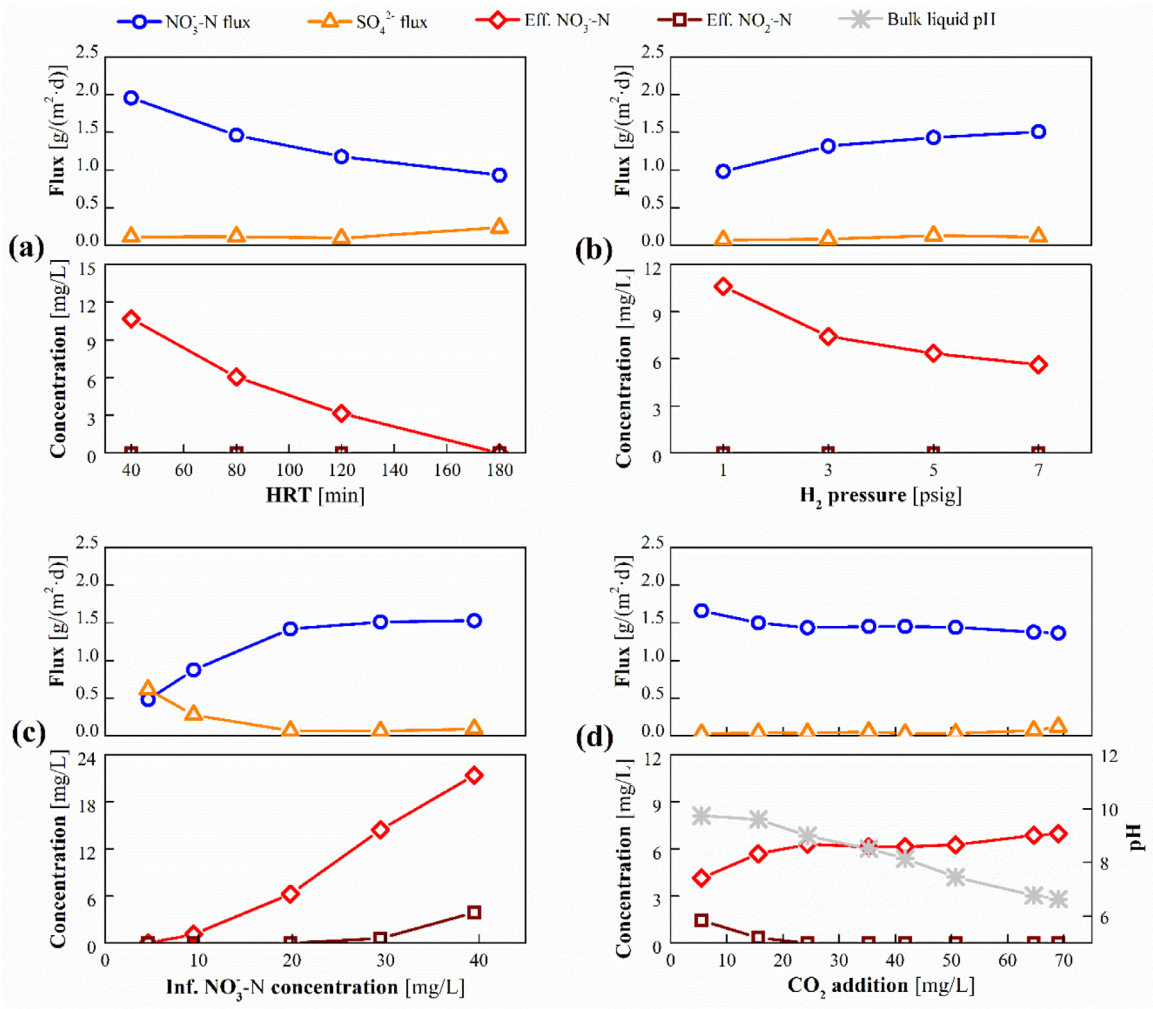

Fig. 2. Effects of (a) HRT (40–180 min), (b) H_2 pressure (1–7 psig), (c) influent NO_3^- concentration (5–40 mg N/L) and (d) CO_2 additon (5.5–69.0 mg/L) on NO_3^- and SO_4^{2-} removal fluxes of the system, NO_3^- and NO_2^- concentrations in the effluents as well as pH of the bulk liquid. Experimental conditions of plots (a)–(d) are shown in Table 1. Note that except for CO_2 series, in other series, bulk liquid pH was controlled at 7.5.

because of the extensive use of these concentrations/pressure in preceding H_2–MBfRs and/or operation safety consideration; in Scenario E5, the measured NO_3^- removal fluxes, NO_3^- and H_2 gradients, effluent DIC concentrations of steady-state system and evolution trend of effluent NO_3^- concentration were used for model validation.

3. Results and discussion

3.1. Experiment-based assessment of denitrification performance

Four series of short-term single-factor experiments were carried out to evaluate the effects of key influence factors such as HRT, H_2 pressure, influent NO_3^- concentration and CO_2 addition on denitrification performance of the CO_2 source H_2–MBfR (Fig. 2). It can be inferred from parts a-d of Fig. 2 that inappropriate selection of operating conditions could give rise to the accelerated SO_4^{2-} reduction (>0.20 g/(m^2·d) and/or NO_2^- accumulation, which are recognized as unwanted processes and should therefore be avoided whenever possible; the optimal operating conditions are as follows: HRT = 80 min, H_2 pressure = 5 psig, influent NO_3^- concentrations = 20 mg N/L and CO_2 addition = 50 mg/L. More detailed analysis concerning the H_2–MBfR performance variation with changing key influence factors can be found in Section S5. Further batch experimental results demonstrate the superiority of CO_2 as the sole carbon source and pH regulator over either bicarbonate (the dominant form of inorganic carbon source in real groundwater) or bicarbonate + phosphate buffer (extensively used pH regulator for H_2–MBfR) (for more details, see Section S6 and Fig. S3). In view of the fact that the denitrification rate of the CO_2 source H_2–MBfR as a function of above influence factors and the advantages of CO_2 addition have been confirmed as above and/or previously suggested (Tang et al., 2011; Xia et al., 2015, 2016), we focus in this study on establishment of an accurate model to give insight to the nature of CO_2-mediated hydrogenotrophic denitrification process, and to serve as an effective prediction tool to guide the design and management of the CO_2 source H_2–MBfR for its prospective application in groundwater treatment.

3.2. Model calibration and evaluation at the optimal operating/simulation conditions

The selected parameters K_m, $K_{CO_2}^{DNB}$ and $K_{CO_2}^{SRB}$ were estimated using AQUASIM built-in iterative algorithms to minimize the sum of squares of the weighted deviations between the experimental measurements and model predictions, detailed calibration information can be found in Section S4. According to sensitivity analysis results (for details, see Section S4), the measured H_2 and NO_3^- gradients within biofilm were insensitive to the changes of $K_{CO_2}^{DNB}$ and

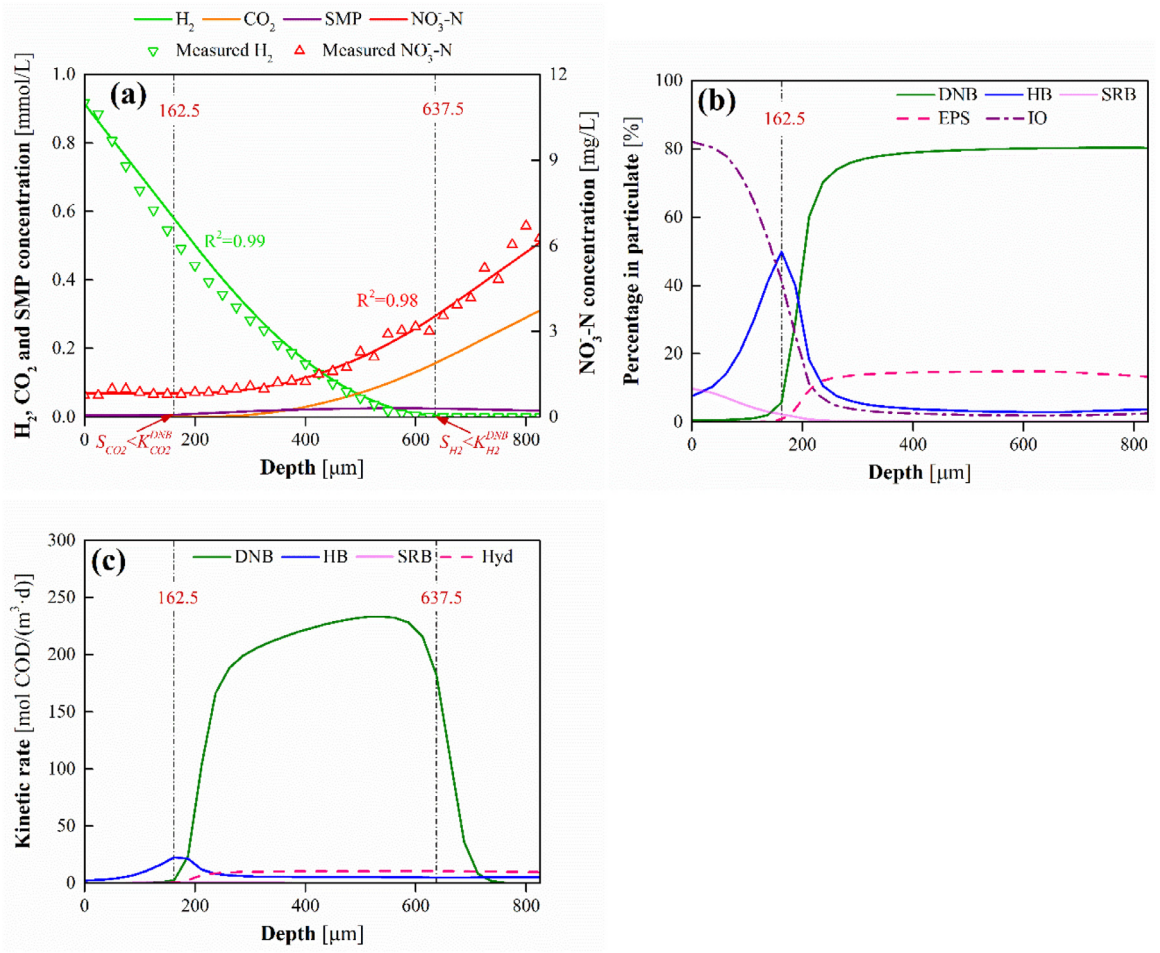

Fig. 3. Model simulation results concerning the characteristics of the steady-state biofilm (Scenario E1): (a) profiles of soluble components, (b) fractions of particulate components and (c) microbial growth rates and hydrolysis rate (k_{hyd}) of EPS along the depth of biofilm. Simulation and operating conditions: biofilm thickness = 825 μm, bulk liquid pH = 7.5, HRT = 80 min, H_2 pressure = 5 psig, CO_2 addition = 50 mg/L and influent NO_3^- and SO_4^{2-} concentration was 20 mg N/L and 20 mg S/L, respectively. Zero point of X axis is membrane side, while depth is the distance from the membrane side.

$K_{CO_2}^{SRB}$ but sensitive to K_m variation (Fig. S2). Similar results were obtained by preceding work that the experimental measurements were insensitive to the changes of half-maximum-rate concentrations (K) of microorganisms for substrates in H_2–MBfR (Tang et al., 2013). In addition to contributing to the commensurable simulated and measured denitrification fluxes (1.45 vs. 1.46 g/(m^2·d)), by calibration of the K_m, $K_{CO_2}^{DNB}$ and $K_{CO_2}^{SRB}$ to reasonable values, the simulated and in situ detected profiles of H_2 and NO_3^- under the optimal operating/simulation conditions could reach a good agreement with the corresponding coefficients of determination (R^2) up to 0.99 and 0.98, respectively, as shown in Fig. 3a. With a high accuracy (which will be further validated later), this model, which was calibrated for the first time based on data relating to concentration gradients of H_2 and NO_3^- in the biofilm of H_2–MBfR, holds the potential to be used as a reliable tool to interpret and predict the denitrification-related behaviors of the CO_2 source H_2–MBfR.

As can be also seen from Fig. 3a, the substrate gradients of the steady-state biofilm with a thickness of 825 ± 25 μm coincide with the typical characteristics of counter-diffusional biofilms (Nerenberg, 2016), namely, the decreased quantity of electron donors (H_2) and acceptors (NO_3^-) with increasing distance from the membrane side (i.e., zero point of depth) and bulk liquid side, respectively; according to the simulated and/or measured profiles, concentrations of NO_3^- (S_{NO3}) across the biofilm were always much higher than $K_{NO_3}^{DNB}$ regardless of depths, while S_{CO2} and S_{H2} were observed to be lower than $K_{CO_2}^{DNB}$ and $K_{H_2}^{DNB}$ at depths below 162.5 μm and beyond 637.5 μm, respectively. The results of particulate components distribution and microbial growth rates in parts b and c of Fig. 3 suggest that a depth of 162.5 μm was the location where the dominant microorganisms were heterotrophic bacteria (HB) with a fraction reaching 49.9% of particulate components, beyond this depth the competitive capacity of HB began to decrease sharply, and the faction and growth rate of DNB started to increase exponentially. In spite of the H_2 limitation at depths of 637.5–825 μm (Fig. 3a), DNB were still the overwhelming microorganisms with a fraction of nearly 80% (Fig. 3b), perhaps due to the relatively higher growth rates of DNB than HB and SRB at depths of 637.5–712.5 μm (Fig. 3c), as well as the outward migration of DNB driven by their fast-growing in the midst of biofilm. The spatial distribution of other components (i.e., inert organics (IO), extracellular polymeric substances (EPS) and soluble microbial products (SMP)) can be explained as follows: as shown in Fig. 3b, the decrease in fraction of IO with increasing depth was ascribed to the increased growth rates of HB and DNB (Fig. 3c), since the growth rate of IO is constant, the increase in the growth rates of other particulate components shall inevitably make IO less competitive for space (Tang et al., 2012); the accumulation of EPS in depths beyond 162.5 μm was incurred by i) the increase in EPS secretion of DNB as a result of the dramatic increased fraction of

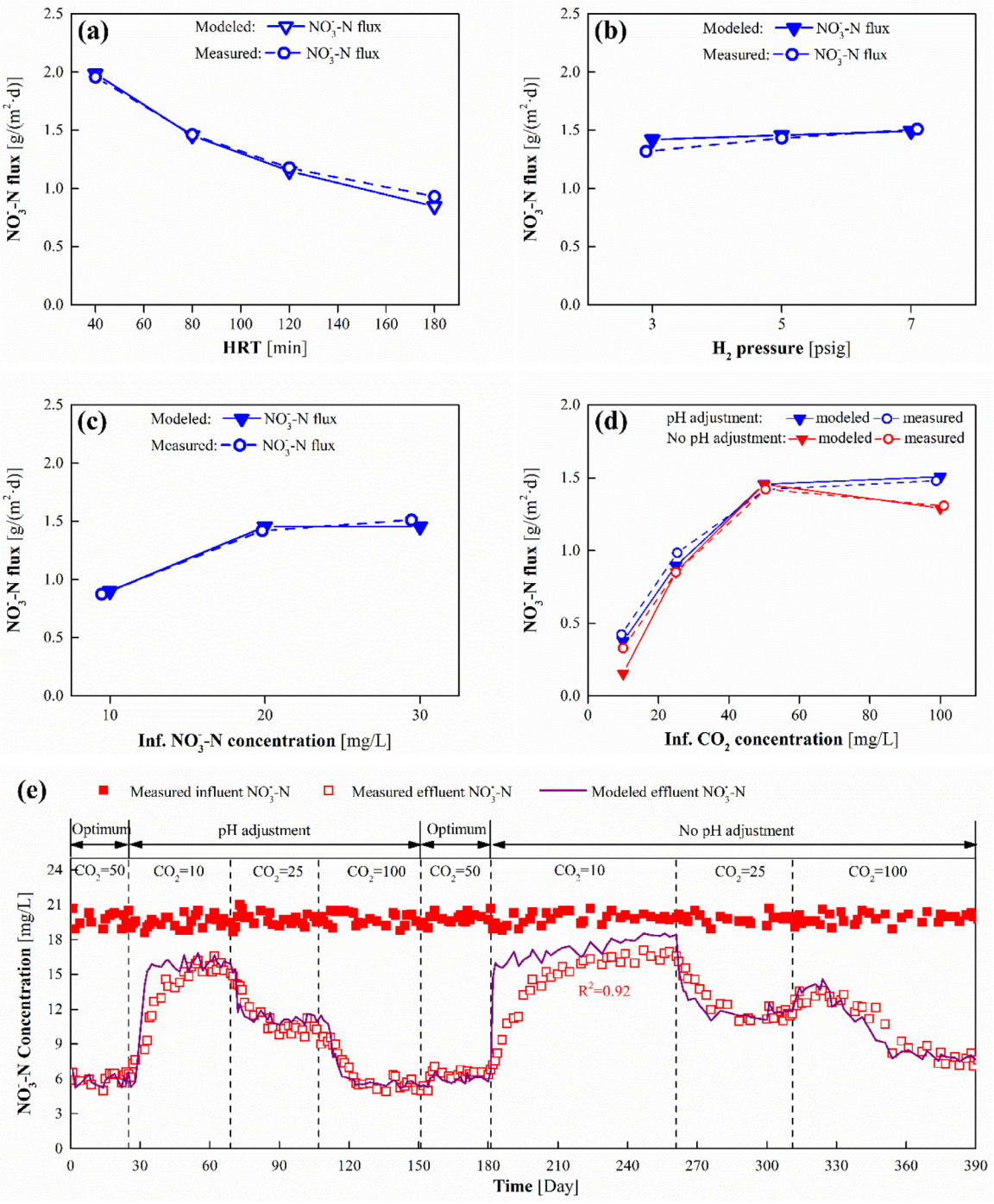

Fig. 4. Comparison of measured and simulated NO_3^- removal fluxes as a function of (a) HRT (40–180 min), (b) H_2 pressure (3–7 psig), (c) influent NO_3^- concentration (10–30 mg N/L), (d) CO_2 addition (10–100 mg/L). For above four series, other experimental and simulation conditions are same as those used in plots (a)–(d) of Fig. 2 and Scenarios E2–E5 of Table S8, respectively. Note that the measured NO_3^- removal fluxes in plots (a)–(c) and plot (d) are the results of short-term and long-term single experiments, respectively. (e) Comparison of measured and simulated evolution trend of effluent NO_3^- concentration as a function of long-term CO_2 addition (10–100 mg/L) with and without pH adjustment. The experimental and simulation conditions in plots (d) and (e) are identical.

DNB (Fig. 3b), and ii) the reduced EPS consumption due to the fact that HB, which grows based on hydrolyzed EPS (i.e., SMP), began to lose their competitive advantage over DNB for space because beyond 162.5 μm carbon source was no longer a limiting factor for DNB growth (Fig. 3a), and as a consequence, suffered the decreased percentages in particulates and growth rates (Fig. 3b and c); the increase of SMP content at depths larger than 162.5 μm was attributed to the increase in fraction and hydrolysis rate of EPS (Fig. 3a and c).

3.3. Model evaluation and validation of the effects of key influence factors

Further simulation was performed to evaluate the impacts of key influence factors (i.e., HRT, H_2 pressure, influent NO_3^- concentration and CO_2 addition) on system performance and biofilm microenvironment. Fig. 4a-d compare the simulated and measured NO_3^- removal fluxes as a function of changing key influence factors. Note that different from HRT, H_2 and NO_3^- series, for CO_2 se-

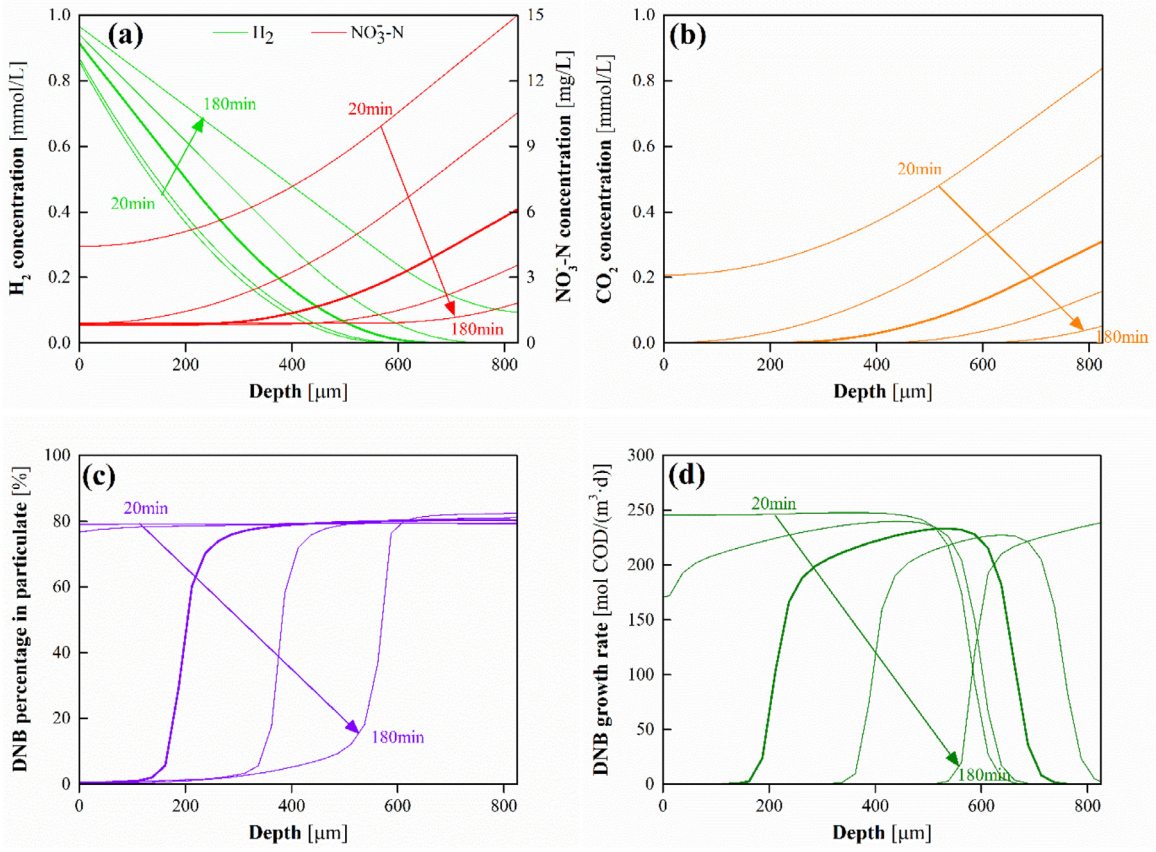

Fig. 5. Model evaluation of (a) profiles of electron donors (H_2) and acceptors (NO_3^-), (b) CO_2 profile, (c) fractions of DNB in particulate components and (d) growth rates of DNB along the depth of biofilm of the system as a function of HRTs ranging from 20 to 180 min (Scenario E2). Simulation conditions: biofilm thickness = 825 μm, bulk liquid pH = 7.5, H_2 pressure = 5 psig, CO_2 addition = 50 mg/L and influent NO_3^- and SO_4^{2-} concentration was 20 mg N/L and 20 mg S/L, respectively. Zero point of X axis is membrane side, while depth is the distance from the membrane side.

ries, the measured NO_3^- removal fluxes in long-term single-factor experiments were adopted to compare the model predictions, since the H_2–MBfR failed to reach steady-state after the operation of short-term (5–7 HRTs) CO_2 addition. It can be seen from parts a-d of Fig. 4 that in most cases, there is a high level of consistency between the measured and simulated NO_3^- removal fluxes. The only exception was for the condition with 10 mg/L CO_2 addition without pH adjustment (Fig. 4d). This is because the resultant bulk liquid pH reached 9.6, which is beyond the effective pH range (below than 8.5) applicable to the normalized Michaelis pH function for prediction of pH-dependent denitrification rates (Estuardo et al., 2008). Fig. 4e plots the effect of long-term CO_2 addition with and without pH adjustment on the time course of the measured and simulated effluent NO_3^- concentration. It is evident that experimental measurements and model predictions coincide well with a R^2 of 0.92, which is comparable to the accuracy of the model outputs of preceding models (R^2 = 0.8–0.99) developed on the same AQUASIM simulation platform (Chen and Ni, 2016; Xu et al., 2014). Fig. S4a-e compare the measured and simulated steady-state H_2 and NO_3^- gradients/profiles as well as effluent DIC concentrations in the case of diverse CO_2 addition with and without pH adjustment. The good agreement between the measured and simulated results in all cases suggests the availability of the calibrated model to predict the utilization capacity of the biofilm for substrates. Taken together, above evidences further validated the high accuracy and reliability of the model.

3.3.1. Model evaluation of the effect of HRT

Fig. 5a and b plot the simulated profiles of substrates including H_2, NO_3^- and CO_2 in the biofilm at HRTs ranging from 20 to 180 min. As the HRT increased, the increasing abundance of H_2 was observed along the depth of biofilm, and the off-gassing of H_2 occurred at a HRT of 180 min (Fig. 5a); while opposite trends were found in NO_3^- and CO_2 profiles, that is, total amounts of NO_3^- and CO_2 in the biofilm decreased with increasing HRT (Fig. 5a and b). This phenomenon is unsurprising given that influent NO_3^- and CO_2 concentrations are invariables, increasing HRT gave rise to the decrease in NO_3^- and CO_2 loadings; while the H_2 loading is unrelated to HRT, but H_2 and NO_3^- are electron donor-acceptor pairs that are always proportionally consumed by DNB, therefore, the decreased NO_3^- loading with increasing HRT inevitably resulted in the increase in the accumulation of H_2 in the biofilm. Fig. 5c shows the fractions of DNB along the depth of biofilm as a function of different HRTs. At a lower HRT (e.g., 20 min), DNB were always the dominant microorganisms in diverse depths of biofilm, which accounted for approximately 80% of particulate components; once the HRT was greater than or equal to 80 min, the inactive zone for denitrification (where the fraction of DNB was lower than 5% of particulate components) formed with its range extended from 0–162.5 μm to 0–412.5 μm as the HRT increased from 80 to 180 min. The decreased quantities of DNB in the biofilm at higher HRTs (80–180 min) were likely due to the increasing degrees of carbon source deficiency that are doubtlessly detrimental to DNB growth in the interior of biofilm (Fig. 5b). This is in accordance with the

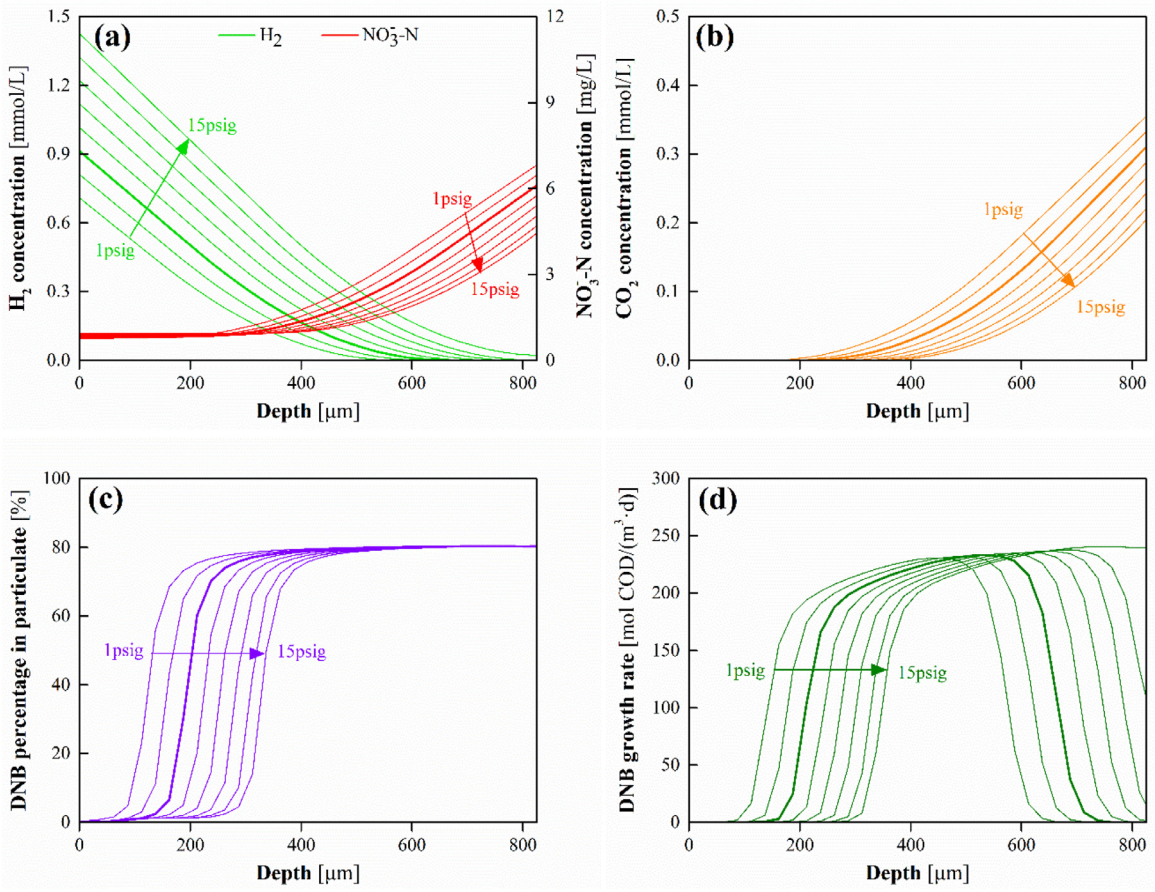

Fig. 6. Model evaluation of (a) profiles of electron donors (H_2) and acceptors (NO_3^-), (b) CO_2 profile, (c) fractions of DNB in particulate components and (d) growth rates of DNB along the depth of biofilm of the system as a function of H_2 pressures ranging from 1 to 15 psig (Scenario E3). Simulation conditions: biofilm thickness = 825 μm, bulk liquid pH = 7.5, HRT = 80 min, CO_2 addition = 50 mg/L and influent NO_3^- and SO_4^{2-} concentration was 20 mg N/L and 20 mg S/L, respectively. Zero point of X axis is membrane side, while depth is the distance from the membrane side.

simulation results of DNB growth rates at varying depths of biofilm in Fig. 5d that at higher HRTs, the growth rates of DNB those were present in the interior of biofilm approached to null. On the basis of model analysis, it can be concluded that increasing HRT could lead to the enlargement of inactive zone for denitrification, which helps explain the experimental results in Fig. 2a that the NO_3^- removal flux of the system decreased with increasing HRT.

3.3.2. Model evaluation of the effect of H_2 pressure

Similar to the effects of different HRTs, increasing H_2 pressure from 1 to 15 psig also caused more abundant accumulation of H_2 and reduced concentrations of NO_3^- and CO_2 in the biofilm, as shown in Fig. 6a and b. Specifically, model outputs in Fig. 6a suggest that a H_2 pressure of 15 psig caused the off-gassing of H_2. This result is inconsistent with our long-term experimental observation as mentioned earlier that the off-gassing of H_2 happened at the H_2 pressure of 7 psig. The discrepancy between simulated and experimental results can be attributed to the fact that in simulation scenario, a 15 psig of H_2 supply exceeded the theoretical demand of microorganisms in the biofilm for electron donors, while for actual scenario, long-term operation of membrane with a 7 psig of H_2 spoiled the membrane structure, and as a consequence, the off-gassing events of H_2. These findings indicate that the development of membrane substratum possessing high anti-pressure capacity is essential to i) improve the consistency of examined and model-predicted results, since the solution of most existing 1-D models was implemented on AQUASIM platform, which, do not consider the impacts of intra-abdominal gas pressure on membrane structure, and ii) take full advantage of the potential of biofilm for H_2 utilization, and consequently more efficient contaminants removal. Owing to the decreasing abundance of CO_2 in the interior of biofilm with increasing H_2 pressure (Fig. 6b), the inactive zone for denitrification was enlarged from 0–112.5 μm at H_2 pressure of 1 psig to 0–337.5 μm at H_2 pressure of 15 psig (Fig. 6c), with this result coinciding with the decreasing tendencies of DNB growth rate with increasing H_2 pressure at same depths in the interior of biofilm, as revealed by Fig. 6d. As can be also found in Fig. 6d, low H_2 pressure resulted in different degrees of DNB growth restriction in the exterior of biofilm; for instance, at a H_2 pressure of 1 psig, the DNB growth rate at the depths of 637.5–825 μm were close to zero. This finding helps explain the increasing NO_3^- removal flux of the system as the H_2 pressure increased (Fig. 2b), though at high H_2 pressure, the growth of DNB in the interior of biofilm was restricted by carbon source deficiency. Given the fact that the unexploited zone of the biofilm where the DNB growth rate approached null existed at the membrane side or bulk liquid side whatever H_2 pressure was employed, the management of biofilm thickness might be the optimal strategy for enhancing the effectiveness of biofilm for contaminants removal.

3.3.3. Model evaluation of the effect of influent NO_3^- concentrations

The simulated profiles of H_2, NO_3^- and CO_2 in the biofilm at influent NO_3^- concentrations ranging from 10 to 30 mg N/L are shown in Fig. 7a and b. The off-gassing of H_2 appeared at influent NO_3^- concentration of 10 mg N/L, likely associated with the lack

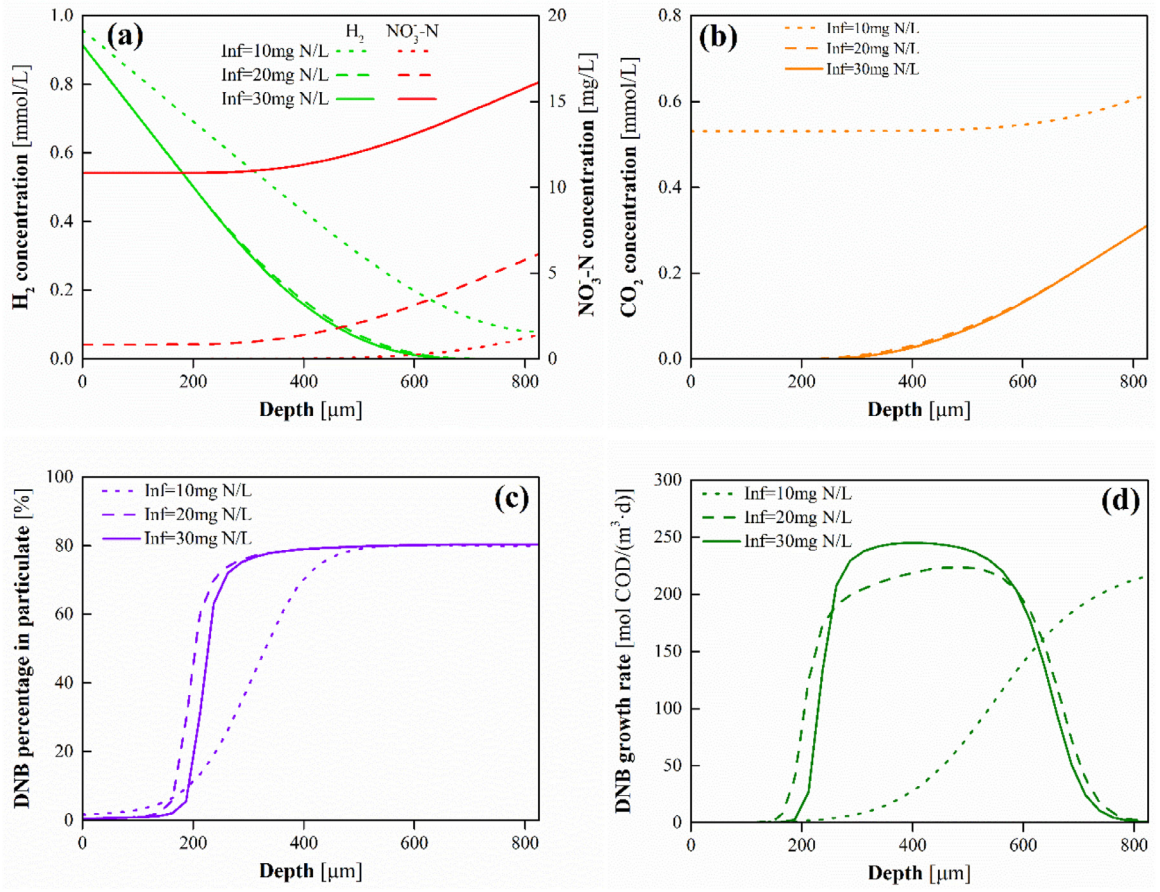

Fig. 7. Model evaluation of (a) profiles of electron donors (H_2) and acceptors (NO_3^-), (b) CO_2 profile, (c) growth rates of DNB and (d) fractions of DNB in particulate components along the depth of biofilm of the system as a function of influent NO_3^--N concentration ranging from 10 to 30 mg N/L (Scenario E4). Simulation conditions: biofilm thickness = 825 μm, bulk liquid pH = 7.5, H_2 pressure = 5 psig, HRT = 80 min, CO_2 addition = 50 mg/L and influent SO_4^{2-} concentration was 20 mg S/L. Zero point of X axis is membrane side, while depth is the distance from the membrane side.

of electron acceptors for DNB in the interior biofilm to consume electron donors (H_2). This is supported by the experimental findings that the SO_4^{2-} removal occurred at influent NO_3^- concentrations of $\leq$ 10 mg N/L (Fig. 2c), in view of the fact that the onset of SO_4^{2-} reduction begins when NO_3^- is almost completely reduced (Tang et al., 2010; Ziv-El and Rittmann, 2009). In the inner layer of biofilm, carbon source deficiency events occurred when influent NO_3^- concentrations of $\geq$ 20 mg N/L were employed (Fig. 7b). Note that the simulated NO_3^- concentrations across the biofilm were significantly increased as the influent NO_3^- concentration was increased from 20 to 30 mg N/L, which can be explained by the biomass limitation of DNB in biofilm. As shown in parts c and d of Fig. 7, despite the similar DNB fractions of the biofilms in the depths of 262.5–587.4 μm at influent NO_3^- concentrations of 20 and 30 mg N/L, the higher DNB growth rates were observed at influent NO_3^- concentrations of 30 mg N/L, implying the increased DNB activity with increasing NO_3^- loading in the central region of biofilm. On the other hand, the increase of DNB activity means the more consumption of H_2 and CO_2 in this region, and consequently the shortening of the coverage range of H_2, CO_2 and DNB in the entire biofilm (Fig. 7a–c). This might be the reason why the growth rate curve of DNB became narrower and steeper as the influent NO_3^- concentrations was increased from 20 to 30 mg N/L. Moreover, in the combination of Figs. 2c and 7d, one can infer that the slow growth rate of DNB induced by the absence of NO_3^- in the interior and central region of biofilm should account for the relatively low NO_3^- removal flux of the system at influent NO_3^- concentration of 10 mg N/L.

3.3.4. Model evaluation of the effect of CO_2 addition

It can be also seen from Fig. 4d that a low addition of CO_2 (e.g., 10 or 25 mg/L) led to an obviously lower NO_3^-removal flux than the optimum CO_2 addition of 50 mg/L, regardless of whether the bulk liquid pH was adjusted (or, in other words, the bulk liquid pH was maintained at 7.5 or without control). The possible underlying mechanism is that the long-term shortage of carbon source led to the decrease in quantity and activity of DNB in the biofilm due to endogenous carbon metabolism. This is supported by the model outputs that in the case of a low addition of CO_2, H_2 and NO_3^- was not completely utilized by the biofilm and CO_2 was scarce in most region of biofilm (Fig. 8a and b), and as a result of carbon source limitation, DNB were not the dominant microorganisms and had no activity (growth rate approached null) at the majority of biofilm depths (Fig. 8c and d). Furthermore, as shown in Fig. 4d, a high addition of carbon source (i.e., CO_2 addition = 100 mg/L) with pH adjustment resulted in a NO_3^- removal flux approximate to that of 50 mg/L CO_2 addition with/without pH adjustment, but obviously higher than that of same carbon addition without pH adjustment (bulk liquid pH =6.1), suggesting the negative impact of excessive CO_2 addition on NO_3^- removal of DNB. This finding is consistent with previous references that a pH below 7.0 usually led to lowered denitrification rates due to the obstruction of microbial function (Ghafari et al., 2010, 2009), and supported by the model outputs that when CO_2 addition was 100 mg/L, no pH adjustment gave rise to the reduced substrates utilization efficiency of biofilm and the decreased growth rates of DNB in the midst of biofilm (Fig. 8a, b and d). Above evidences allow us to conclude

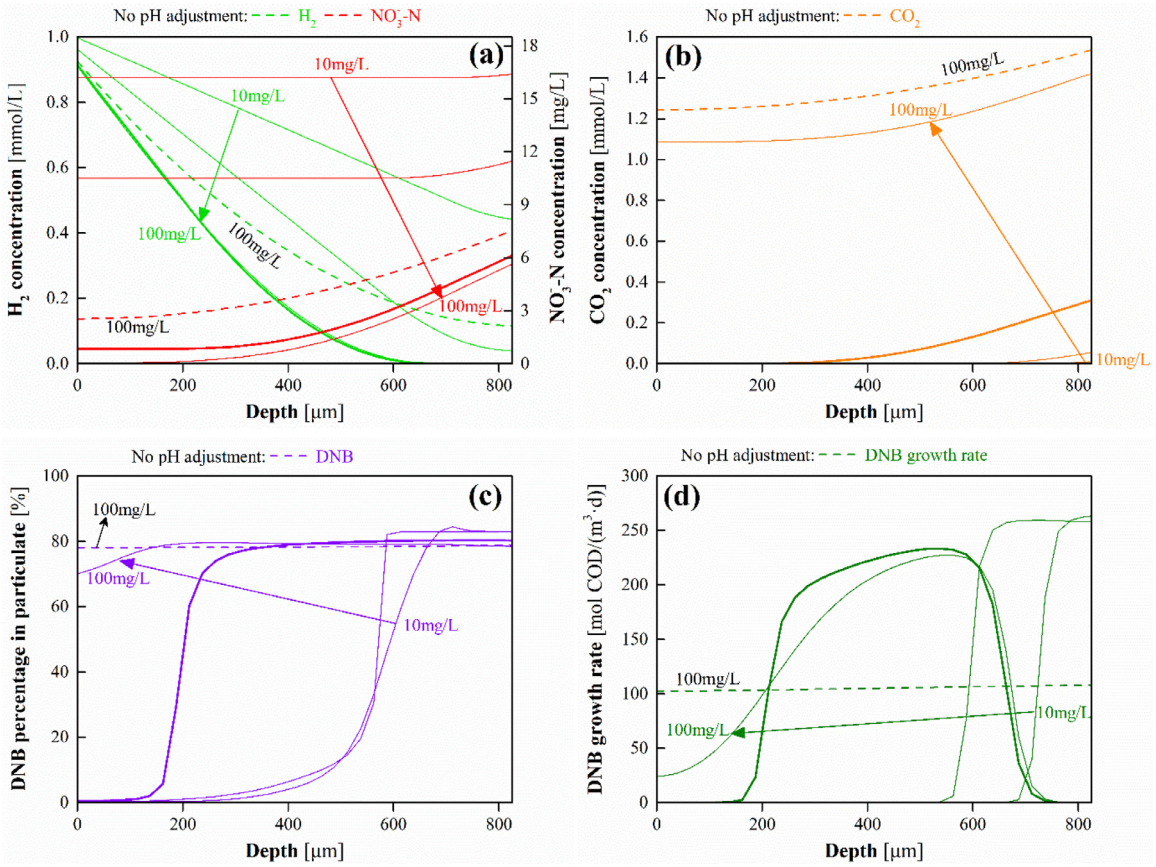

Fig. 8. Model evaluation of (a) profiles of electron donors (H_2) and acceptors (NO_3^-), (b) CO_2 profile, (c) fractions of DNB in particulate components and (d) growth rates of DNB along the depth of biofilm of the system as a function of CO_2 addition ranging from 10 to 100 mg/L (Scenario E5). Simulation conditions: biofilm thickness = 825 μm, H_2 pressure = 5 psig, HRT = 80 min, and influent NO_3^- and SO_4^{2-} concentration was 20 mg N/L and 20 mg S/L, respectively. In Fig. 8a–d, solid lines represent the simulation results in the cases that different concentration of CO_2 was added and bulk liquid pH was maintained at 7.5, dash lines refer to the simulation results when 100 mg/L CO_2 was added and bulk liquid pH was not adjusted; zero point of X axis is membrane side, while depth is the distance from the membrane side.

that the dominant role of CO_2 in mediating hydrogenotrophic denitrification process was depending on CO_2 concentration, given that carbon source and bulk liquid pH was the main limiting factor for NO_3^- removal rate of DNB in the case of CO_2 addition below and beyond 50 mg/L, respectively; CO_2 addition should be cautiously considered and precisely controlled because more or less CO_2 addition was detrimental to maintaining high denitrification performance of the H_2–MBfR.

3.4. Model evaluation of the effect of biofilm thickness

As have been pointed out by preceding references (Martin et al., 2013; Wu et al., 2018), insufficient and excessive thick biofilms always lead to unsatisfactory NO_3^- removal fluxes of H_2–MBfR due to biomass and/or substrate limitation. In this sense, exploring the optimal biofilm thickness is of great importance to full exploitation of denitrification potential of CO_2 source H_2–MBfR, in view of the possible discrepancy between the practical and desirable thickness of biofilm. Fig. 9a–c plot the simulated concentrations of H_2, NO_3^- and CO_2 and DNB growth rates in the biofilm at postulated biofilm thicknesses ranging from 200 to 1000 μm. It is evident that i) NO_3^- concentrations across the biofilms were not the decision factor for restriction of DNB growth in all biofilms with diverse thickness; ii) biofilms with higher thickness (e.g., 800 and 1000 μm) suffered from low DNB growth rates in the outer region of biofilms, and a biofilm thickness of 650 μm contributed to relatively high DNB growth rates in most regions of biofilm on the premise that H_2 utilization efficiency approached 100%, while the biofilm thicknesses of 200–600 μm resulted in wasting H_2 concentrations of 38.1–1559.8 μg/L, orders of magnitude high than the recommended liquid-phase H_2 concentration (9 μg/L) in H_2–MBfR (Lee and Rittmann, 2002); iii) the carbon deficiency events appeared and became the main limiting factor for DNB growth in the inner region of biofilms at biofilm thicknesses of ≥ 400 μm.

Fig. 9d compares the NO_3^- removal fluxes at diverse biofilm thicknesses with the result showing the highest denitrification rate at a biofilm thickness of 600 μm. Despite this, the 650 μm was regarded as the optimal biofilm thickness considering that the biofilm thickness of 650 μm contributed to a relatively high NO_3^- removal flux of 1.59 g/(m^2·d), which is merely decreased by 2.4% compared to that at 600 μm, but led to the complete utilization of H_2, which can avoid electron wasting and formation of explosive atmosphere issues (Lee and Rittmann, 2002). Moreover, it is noticeable that compared to the experimentally determined denitrification rate (1.46 g/(m^2·d)) at same conditions, the NO_3^- removal flux of the system could be further increased by 9.1% theoretically if the thickness of biofilm was decreased from 825 μm to 650 μm. The characteristics of microbial structure within biofilm at different thicknesses ranging from 200 to 1000 μm are shown in Fig. 10. For thin biofilms with thickness below 475 μm, DNB was the dominant microorganisms (accounting for nearly 80% of particulate components), as outlined in Fig. 10a–c. The relatively low NO_3^- removal flux of thin biofilms shown in Fig. 9d can be attributed to the biomass limitation. While for the thick biofilms with thickness higher than 475 μm (e.g., 650–1000 μm), DNB growth was subject to the greater diffusional resistance of substrates, for in-

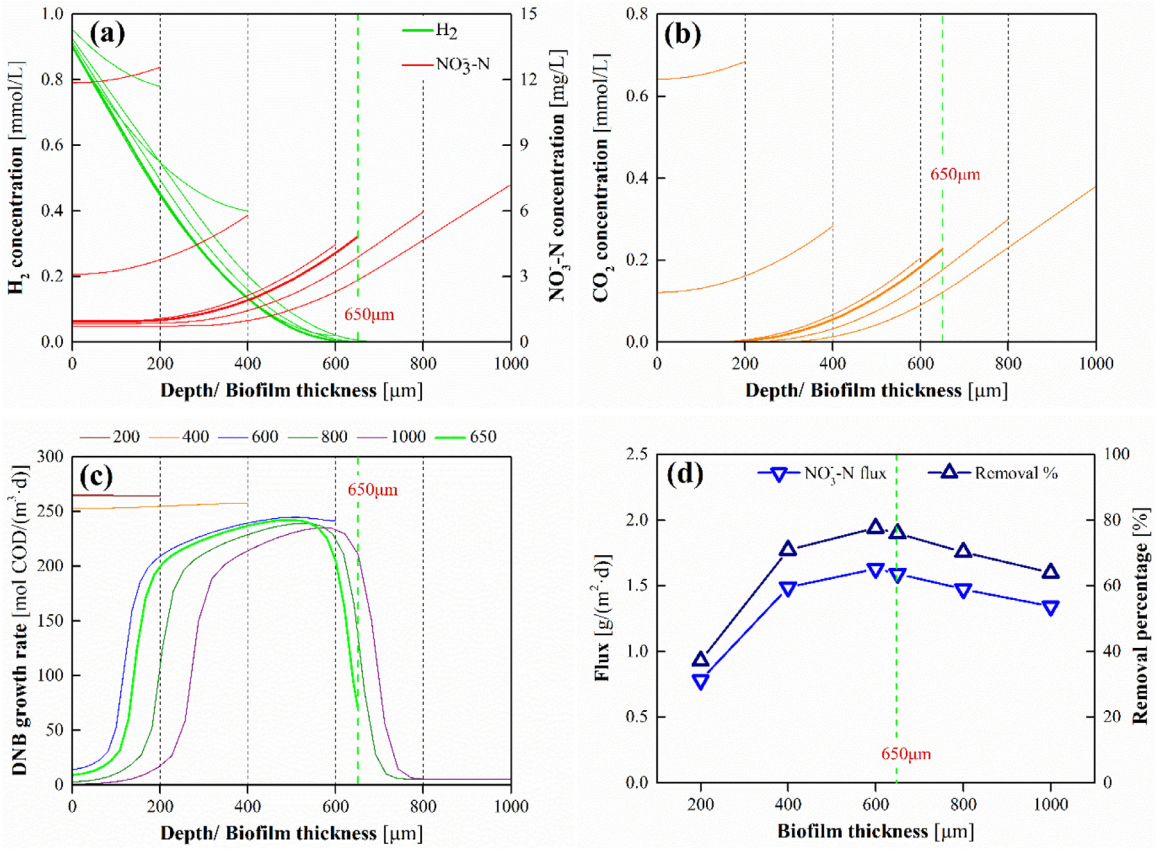

Fig. 9. Model evaluation of (a) H_2 and NO_3^- and (b) CO_2 profiles, (c) growth rates of DNB along the depth of biofilms, and (d) NO_3^- removal fluxes of the system as a function of biofilm thicknesses ranging from 200 to 1000 μm (Scenario E6). Simulation conditions: bulk liquid pH = 7.5, H_2 pressure = 5 psig, HRT = 80 min, CO_2 addition = 50 mg/L and influent NO_3^- and SO_4^{2-} concentration was 20 mg N/L and 20 mg S/L, respectively. Zero point of X axis is membrane side, while depth is the distance from the membrane side.

stance, SRB and/or HB overcame DNB for space in the inner region of biofilm due to the limited inward transfer of CO_2 (Fig. 10d-f); in particular, despite the highest fractions of DNB in the outer region of biofilm, those DNB possessed low growth rate due to the limited outward transfer of H_2, as illustrated by combined analysis of Fig. 9c and Fig. 10d-f. These evidences help interpret the decline in NO_3^- removal flux of the system with increasing biofilm thickness at biofilm thickness higher than 600 μm.

3.5. Implications of this work and research opportunities

This study was undertaken to evaluate the process performance and give insight into the nature of the interaction mechanisms of microorganisms in the biofilm of a novel CO_2 source H_2–MBfR system. The optimization design of the set-up configuration was realized by linking the H_2–MBfR to a separated CO_2 providing system for more precise CO_2 addition, and to a versatile microsensor measuring unit which can provide in situ collected data that can be not only used for the mathematical model development, but offering guidance to the management of the H_2–MBfR if it is applied for real groundwater treatment. A more sophisticated model was established for capturing the microbial behaviors in the CO_2-mediated hydrogenotrophic denitrification process, expanded by consideration of the synchronous effects of inorganic carbon source and bulk liquid pH on the microbial metabolic process kinetics of microorganisms, and calibrated by comparison of the measurements (i.e., substrates gradients in the biofilm of the H_2–MBfR) of the microsensor measuring unit and the model predictions. The model was validated to own a high accuracy in predicting the system performance in different simulation scenarios, and have better application potential for describing denitrification process in H_2–MBfR when compared with the one without considering the impacts of inorganic carbon source (for details, see Section S7 and Fig. S5). In addition, this work bridged the knowledge gap in evolution trends of biofilm microenvironment when CO_2 was utilized as inorganic carbon source and/or pH regulator of a H_2–MBfR.

It is worth mentioning that although the optimal biofilm thickness for a H_2–MBfR can be deduced by the developed model, it is still of great importance to undertake further experimental research for verifying whether the most efficient NO_3^- removal can be achieved as the biofilm is controlled at the predicted optimal thickness, by means of the well-established physicochemical approaches for biofilm thickness management (e.g., intermittent ultrasound treatment (Lee and Rittmann, 2002) and chemical reagents dosage (Splendiani et al., 2006)). In order to further our understanding of the impacts of key influence factors on the H_2–MBfR performance, more efforts should be paid to simulate the performance variation of the system with the simultaneous change of multiple influence factors using the proposed model. Meanwhile, the generalization ability of the proposed model (i.e., the applicability to simulate the microbial metabolic processes for other pollutants removal in diverse biofilm systems) also merits further evaluation in the future study. Additionally, effective method for in situ monitoring of CO_2 concentration in the biofilm is yet to be developed, which is conductive to providing direct evidence for spatial distribution of carbon source that can be used to calibrate biofilm model and guide the operation of H_2–MBfR.

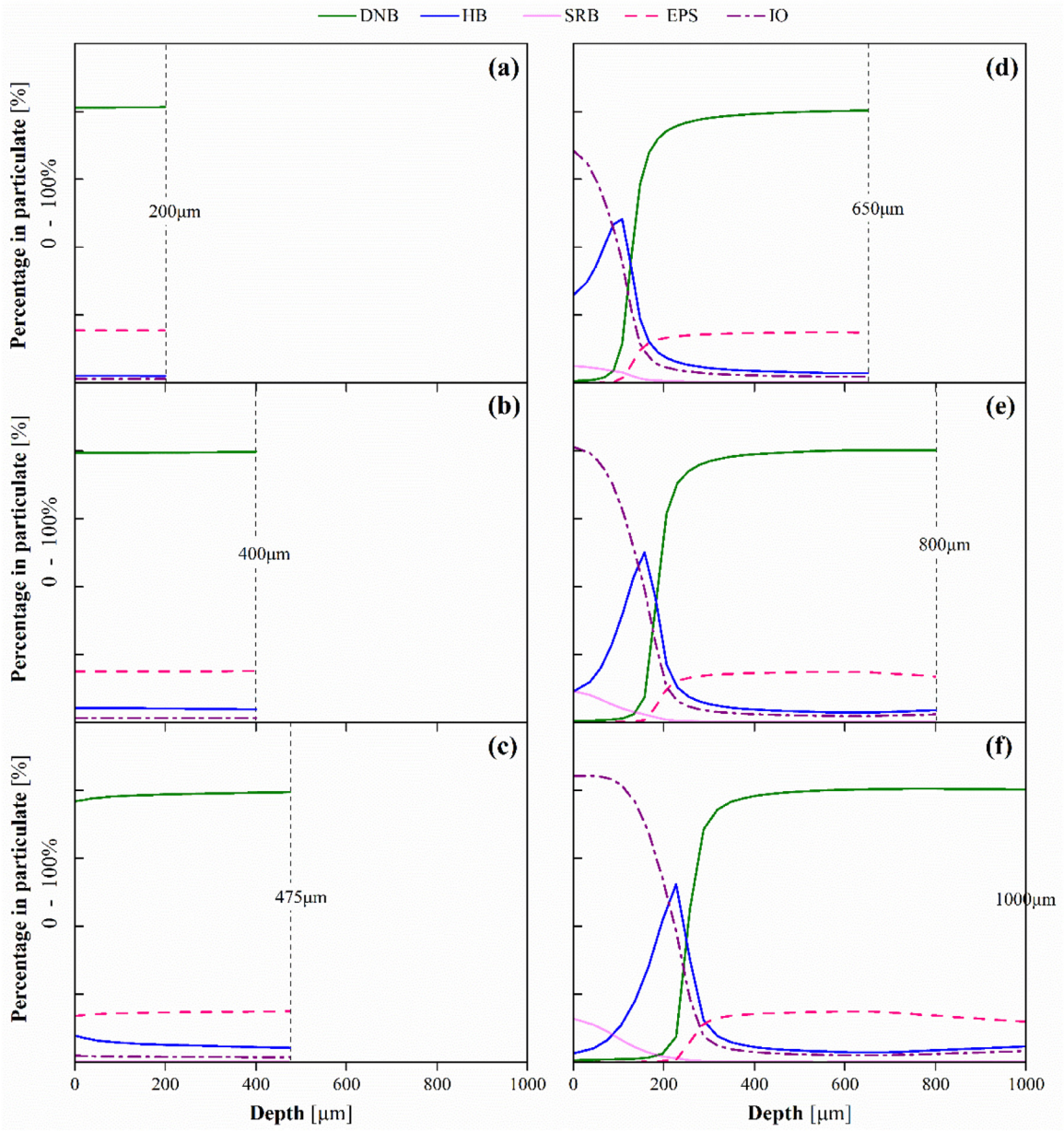

Fig. 10. Model simulation results concerning the fractions of particulate components along the depth of biofilms with thickness of (a) 200 μm, (b) 400 μm, (c) 475 μm, (d) 650 μm, (e) 800 μm and (f) 1000 μm (Scenario E6). Simulation conditions: bulk liquid pH = 7.5, H_2 pressure = 5 psig, HRT = 80 min, CO_2 addition = 50 mg/L and influent NO_3^- and SO_4^{2-} concentration was 20 mg N/L and 20 mg S/L, respectively. Zero point of X axis is membrane side, while depth is the distance from the membrane side.

4. Conclusions

A novel H_2−MBfR integrating a microsensor measuring unit for in situ detection of electron donors (H_2) and acceptors (NO_3^-) concentrations gradients within biofilm and a separated CO_2 providing system for carbon source addition and pH control was developed and experimentally proved to possess the optimal denitrification performance and minimized undesirable processes at HRT 80 min, influent NO_3^- concentration 20 mg N/L, H_2 pressure 5 psig and CO_2 addition 50 mg/L. Following batch experiments further demonstrates the superiority of CO_2 as the unique carbon source and pH regulator. For in-depth illustration of the denitrification-related mechanisms, a model with expanded microbial metabolic process kinetics and high fidelity was proposed, calibrated and validated by comparing the simulated and measured system performance and/or substrate gradients within biofilm under different simulation scenarios, and the optimization of parameters including K_m, $K_{CO_2}^{DNB}$ and $K_{CO_2}^{SRB}$. Simulation results reveal the biofilm microenvironment evolutions with changing key influence factors, which can mechanistically explain the short-term or long-term single-factor experimental findings that the macroscale process performance of the H_2−MBfR was sensitive to HRT, H_2 pressure and influent NO_3^- concentration and CO_2 addition; the optimum biofilm thickness was predicted to be 650 μm which guarantees a relatively high denitrification flux while avoiding the off-gassing of H_2. Owing to the advantages involving the precise supply of CO_2 and online monitoring of biofilm microenvironment, the developed system with good reliability and flexibility may serve as an attractive candidate for NO_3^- removal from groundwater, and the proposed model offers a powerful tool to guide the maintaining and management of the system.

Declaration of Competing Interest

The authors declare that they have no known competing financial interests or personal relationships that could have appeared to influence the work reported in this paper.

Acknowledgment

This work was supported by the National Natural Science Foundation of China (51878197; 51768012), Innovation Project of Guangxi Graduate Education (YCBZ2017053), Guangxi Science and Technology Planning Project (GuiKe-AD18126018), and Guangxi Collaborative Innovation Center for Water Pollution Control and Water Safety in Karst Area.

Supplementary materials

Supplementary material associated with this article can be found, in the online version, at doi:10.1016/j.watres.2020.116177.

References

Byrne, R.H., 2014. Measuring ocean acidification: new technology for a new era of ocean chemistry. Environ. Sci. Technol. 48 (10), 5352–5360. https://doi.org/10.1021/es405819p.

Cecconet, D., Devecseri, M., Callegari, A., Capodaglio, A.G., 2018. Effects of process operating conditions on the autotrophic denitrification of nitrate-contaminated groundwater using bioelectrochemical systems. Sci. Total Environ. 613-614, 663–671. https://doi.org/10.1016/j.scitotenv.2017.09.149.

Chen, X., Lai, C.-Y., Fang, F., Zhao, H.-P., Dai, X., Ni, B.-J., 2019. Model-based evaluation of selenate and nitrate reduction in hydrogen-based membrane biofilm reactor. Chem. Eng. Sci. 195, 262–270. https://doi.org/10.1016/j.ces.2018.11.032.

Chen, X., Ni, B.-J., 2016. Anaerobic conversion of hydrogen and carbon dioxide to fatty acids production in a membrane biofilm reactor: a modeling approach. Chem. Eng. J. 306, 1092–1098. https://doi.org/10.1016/j.cej.2016.08.049.

Chung, J., Nerenberg, R., Rittmann, B.E., 2007. Evaluation for biological reduction of nitrate and perchlorate in brine water using the hydrogen-based membrane biofilm reactor. J. Environ. Eng. 133 (2), 157–164. https://doi.org/10.1061/(ASCE)0733-9372(2007)133:2(157).

Estuardo, C., Martí, M.C., Huiliñir, C., Aspé Lillo, E., Roeckel von Bennewitz, M., 2008. Improvement of nitrate and nitrite reduction rates prediction. Electron. J. Biotechnol. 11, 73–82. https://doi.org/10.2225/vol11-issue3-fulltext-6.

Gao, S., Li, C., Jia, C., Zhang, H., Guan, Q., Wu, X., Wang, J., Lv, M., 2020. Health risk assessment of groundwater nitrate contamination: a case study of a typical karst hydrogeological unit in East China. Environ. Sci. Pollut. R. 27 (9), 9274–9287. https://doi.org/10.1007/s11356-019-07075-w.

Ghafari, S., Hasan, M., Aroua, M.K., 2009. Effect of carbon dioxide and bicarbonate as inorganic carbon sources on growth and adaptation of autohydrogenotrophic denitrifying bacteria. J. Hazard. Mater. 162 (2), 1507–1513. https://doi.org/10.1016/j.jhazmat.2008.06.039.

Ghafari, S., Hasan, M., Aroua, M.K., 2010. A kinetic study of autohydrogenotrophic denitrification at the optimum pH and sodium bicarbonate dose. Bioresour. Technol. 101 (7), 2236–2242. https://doi.org/10.1016/j.biortech.2009.11.068.

Gu, B., Ying, G., Chang, S.X., Luo, W., Jie, C., 2013. Nitrate in groundwater of China: sources and driving forces. Global Environ. Chang. 23 (5), 1112–1121. https://doi.org/10.1016/j.gloenvcha.2013.05.004.

Hach, Company., 1992. Hach Water Analysis Handbook. Hach Company.

Karanasios, K.A., Vasiliadou, I.A., Pavlou, S., Vayenas, D.V., 2010. Hydrogenotrophic denitrification of potable water: a review. J. Hazard. Mater. 180 (1), 20–37. https://doi.org/10.1016/j.jhazmat.2010.04.090.

Lai, C.Y., Yang, X., Tang, Y., Rittmann, B.E., Zhao, H.-P., 2014. Nitrate shaped the selenate-reducing microbial community in a hydrogen-based biofilm reactor. Environ. Sci. Technol. 48 (6), 3395–3402. https://doi.org/10.1021/es4053939.

Lee, K.C., Rittmann, B.E., 2002. Applying a novel autohydrogenotrophic hollow-fiber membrane biofilm reactor for denitrification of drinking water. Water Res. 36 (8), 2040–2052. https://doi.org/10.1016/S0043-1354(01)00425-0.

Lee, K.C., Rittmann, B.E., 2003. Effects of pH and precipitation on autohydrogenotrophic denitrification using the hollow-fiber membrane-biofilm reactor. Water Res. 37 (7), 1551–1556. https://doi.org/10.1016/S0043-1354(02)00519-5.

Lee, K.C., Rittmann, B.E., 2000. A novel hollow-fibre membrane biofilm reactor for autohydrogenotrophic denitrification of drinking water. Water Sci. Technol. 41 (4–5), 219–226. https://doi.org/10.2166/wst.2000.0448.

Lewandowski, Z., Beyenal, H., 2013. Fundamentals of Biofilm Research. CRC press.

Liu, Y., Wang, J., 2019. Reduction of nitrate by zero valent iron (ZVI)-based materials: a review. Sci. Total Environ. 671, 388–403. https://doi.org/10.1016/j.scitotenv.2019.03.317.

Martin, K.J., Nerenberg, R., 2012. The membrane biofilm reactor (MBfR) for water and wastewater treatment: principles, applications, and recent developments. Bioresour. Technol. 122, 83–94. https://doi.org/10.1016/j.biortech.2012.02.110.

Martin, K.J., Picioreanu, C., Nerenberg, R., 2013. Multidimensional modeling of biofilm development and fluid dynamics in a hydrogen-based, membrane biofilm reactor (MBfR). Water Res. 47 (13), 4739–4751. https://doi.org/10.1016/j.watres.2013.04.031.

Nerenberg, R., 2016. The membrane-biofilm reactor (MBfR) as a counter-diffusional biofilm process. Curr. Opin. Biotechnol. 38, 131–136. https://doi.org/10.1016/j.copbio.2016.01.015.

Nerenberg, R., Rittmann, B.E., 2004. Hydrogen-based, hollow-fiber membrane biofilm reactor for reduction of perchlorate and other oxidized contaminants. Water Sci. Technol. 49 (11–12), 223–230. https://doi.org/10.2166/wst.2004.0847.

Ontiveros-Valencia, A., Ziv-El, M., Zhao, H.-P., Feng, L., Rittmann, B.E., Krajmalnik-Brown, R., 2012. Interactions between nitrate-reducing and sulfate-reducing bacteria coexisting in a hydrogen-fed biofilm. Environ. Sci. Technol. 46 (20), 11289–11298. https://doi.org/10.1021/es302370t.

Qiu, J., 2011. China to spend billions cleaning up groundwater. Science 334 (6057), 745. https://doi.org/10.1126/science.334.6057.745.

Reichert, P., 1994. AQUASIM—a tool for simulation and data analysis of aquatic systems. Water Sci. Technol. 30 (2), 21–30. https://doi.org/10.2166/wst.1994.0025.

Rittmann, B.E., McCarty, P.L., 2012. Environmental biotechnology: Principles and Applications. Tata McGraw-Hill Education.

Sahu, A.K., Sengupta, S., Ergas, S.J., 2009. Onsite wastewater denitrification using a hydrogenotrophic hollow-fiber membrane bioreactor. Water Environ. Res. 81 (7), 680–686. https://doi.org/10.2175/106143008x370322.

Sevda, S., Sreekishnan, T.R., Pous, N., Puig, S., Pant, D., 2018. Bioelectroremediation of perchlorate and nitrate contaminated water: a review. Bioresour. Technol. 255, 331–339. https://doi.org/10.1016/j.biortech.2018.02.005.

Splendiani, A., Livingston, A.G., Nicolella, C., 2006. Control of membrane-attached biofilms using surfactants. Biotechnol. Bioeng. 94 (1), 15–23. https://doi.org/10.1002/bit.20752.

Stumm, W., Morgan, J.J., 1996. Aquatic Chemistry: Chemical Equilibria and Rates in Natural Waters. John Wiley & Sons.

Su, X., Wang, H., Zhang, Y., 2013. Health risk assessment of nitrate contamination in groundwater: a case study of an agricultural area in Northeast China. Water Resour. Manag. 27 (8), 3025–3034. https://doi.org/10.1007/s11269-013-0330-3.

Tang, Y., Ontiveros-Valencia, A., Feng, L., Zhou, C., Krajmalnik-Brown, R., Rittmann, B.E., 2013. A biofilm model to understand the onset of sulfate reduction in denitrifying membrane biofilm reactors. Biotechnol. Bioeng. 110 (3), 763–772. https://doi.org/10.1002/bit.24755.

Tang, Y., Zhao, H., Marcus, A.K., Krajmalnik-Brown, R., Rittmann, B.E., 2012. A steady-state biofilm model for simultaneous reduction of nitrate and perchlorate, part 1: model development and numerical solution. Environ. Sci. Technol. 46 (3), 1598–1607. https://doi.org/10.1021/es203129s.

Tang, Y., Zhou, C., Ziv-El, M., Rittmann, B.E., 2011. A pH-control model for heterotrophic and hydrogen-based autotrophic denitrification. Water Res. 45 (1), 232–240. https://doi.org/10.1016/j.watres.2010.07.049.

Tang, Y., Ziv-El, M., Zhou, C., Shin, J.H., Ahn, C.H., Meyer, K., Candelaria, D., Friese, D., Overstreet, R., Scott, R., Rittmann, B.E., 2010. Bioreduction of nitrate in groundwater using a pilot-scale hydrogen-based membrane biofilm reactor. Front. Environ. Sci. Eng. China 4 (3), 280–285. https://doi.org/10.1007/s11783-010-0235-9.

Wakida, F.T., Lerner, D.N., 2005. Non-agricultural sources of groundwater nitrate: a review and case study. Water Res. 39 (1), 3–16. https://doi.org/10.1016/j.watres.2004.07.026.

Wu, J., Yin, Y., Wang, J., 2018. Hydrogen-based membrane biofilm reactors for nitrate removal from water and wastewater. Int. J. Hydrogen Energy 43 (1), 1–15. https://doi.org/10.1016/j.ijhydene.2017.10.178.

Xia, S., Liang, J., Xu, X., Shen, S., 2013. Simultaneous removal of selected oxidized contaminants in groundwater using a continuously stirred hydrogen-based membrane biofilm reactor. J. Environ. Eng. 25 (1), 96–104. https://doi.org/10.1016/S1001-0742(12)60013-8.

Xia, S., Wang, C., Xu, X., Tang, Y., Wang, Z., Gu, Z., Zhou, Y., 2015. Bioreduction of nitrate in a hydrogen-based membrane biofilm reactor using CO_2 for pH control and as carbon source. Chem. Eng. J. 276, 59–64. https://doi.org/10.1016/j.cej.2015.04.061.

Xia, S., Xu, X., Zhou, C., Wang, C., Zhou, L., Rittmann, B.E., 2016. Direct delivery of CO_2 into a hydrogen-based membrane biofilm reactor and model development. Chem. Eng. J. 290, 154–160. https://doi.org/10.1016/j.cej.2016.01.021.

Xia, S., Zhong, F., Zhang, Y., Li, H., Yang, X., 2010. Bio-reduction of nitrate from groundwater using a hydrogen-based membrane biofilm reactor. J. Environ. Sci.-China 22 (2), 257–262. https://doi.org/10.1016/S1001-0742(09)60102-9.

Xu, X., Chen, C., Wang, A., Guo, W., Zhou, X., Lee, D.-J., Ren, N., Chang, J.-S., 2014. Simultaneous removal of sulfide, nitrate and acetate under denitrifying sulfide removal condition: modeling and experimental validation. J. Hazard. Mater. 264 (Supplement C), 16–24. https://doi.org/10.1016/j.jhazmat.2013.10.056.

Zhao, H.P., Ilhan, Z.E., Ontiveros-Valencia, A., Tang, Y., Rittmann, B.E., Krajmalnik-Brown, R., 2013a. Effects of multiple electron acceptors on microbial interactions in a hydrogen-based biofilm. Environ. Sci. Technol. 47 (13), 7396–7403. https://doi.org/10.1021/es401310j.

Zhao, H.P., Ontiveros-Valencia, A., Tang, Y., Kim, B.-O., VanGinkel, S., Friese, D., Overstreet, R., Smith, J., Evans, P., Krajmalnik-Brown, R., Rittmann, B., 2014. Removal of multiple electron acceptors by pilot-scale, two-stage membrane biofilm reactors. Water Res. 54, 115–122. https://doi.org/10.1016/j.watres.2014.01.047.

Zhao, H.P., Ontiveros-Valencia, A., Tang, Y., Kim, B.O., Ilhan, Z.E., Krajmalnik-Brown, R., Rittmann, B., 2013b. Using a two-stage hydrogen-based membrane biofilm reactor (MBfR) to achieve complete perchlorate reduction in the presence of nitrate and sulfate. Environ. Sci. Technol. 47 (3), 1565–1572. https://doi.org/10.1021/es303823n.

Ziv-El, M.C., Rittmann, B.E., 2009. Systematic evaluation of nitrate and perchlorate bioreduction kinetics in groundwater using a hydrogen-based membrane biofilm reactor. Water Res. 43 (1), 173–181. https://doi.org/10.1016/j.watres.2008.09.035.